Supporting Information for "Simulated slidequakes: Insights from DPM simulations into the high-frequency seismic signal generated by geophysical granular flows"

M. I. Arran[1*], A. Mangeney[1], J. De Rosny[2], R. Toussaint[3,4]

[1]Université de Paris, Institut de physique du globe de Paris, CNRS, F-75005 Paris, France

[2]Institut Langevin, ESPCI Paris, PSL University, CNRS, 75005 Paris, France

[3]Université de Strasbourg, CNRS, Institut Terre et Environnement de Strasbourg, UMR 7063, F-67084 Strasbourg, France

[4]SFF PoreLab, The Njord Centre, Department of Physics, University of Oslo, Oslo, Norway

[*]Corresponding author: Matthew Arran, mia31@cantab.ac.uk

Contents of this file

1. Text S1 to S8
2. Figures S1 to S8
3. Table S1

Additional Supporting Information (Files uploaded separately)

1. Captions for Movies S1 to S3

0148-0227/23/$9.00

Introduction

To supplement the text of "Simulated Landquakes", we gather here a collection of eight appendices to the text; seven figures and a table associated with these appendices; and descriptions of three videos that provide supplementary illustration.

In section S1, we list and define the notation used in the article's text. Section S2 justifies our neglect of plastic yield in simulating interparticle interactions, as described in section 1.2, while section S3 describes the interparticle interactions that we simulate, and section S4 explains our calibration of those interactions' parameters. Section S5 describes our use of coarse-graining to calculate continuous mean flow properties from the properties of discrete simulated particles, while section S6 describes our derivation of a theoretical power spectrum for the normal interparticle force exerted during a Hertzian collision. Finally, section S7 considers the geometry of force transmission by interparticle collisions, and section S8 considers the effect of the simulated domain size on our results.

Figure S1 is associated with section S2; Figures S2, S3, S4, and S5 with sections S4.1, S4.2, S4.4, and S4.5; and Figure S6 with section S6. Figure S7 is associated with section S7 and Figure S8 with section S8. Finally, the mpeg4 videos available as supplementary material illustrate sections 2.2 and 4.3 and are described at Movie S1, Movie S2, and Movie S3.

S1. Notation

x, y, z: Downslope, cross-slope, & base-normal positions

f, t: Frequency and time co-ordinates

ρ, d: Particles' density and typical diameter

g, θ: The magnitude of gravitational acceleration and its angle to the base's normal

n_x, n_y: The numbers of typical particles required to span the domain, downslope and cross-slope

A, n_z: The basal area analyzed and the base-normal number of particles overlying each point of it

$t_0, \Delta t$: The start time and duration of the period of steady flow we analyze

δt: The simulation timestep

ν, E, G: The Poisson's ratio, Young's modulus, and shear modulus for particles

ν_w, E_w, G_w: The Poisson's ratio, Young's modulus, and shear modulus for the channel wall

δ_n, δ_t: Normal and tangential displacements, from equilibrium, of an interparticle contact's midpoint

θ_n, θ_r: Torsional and roll-induced angular displacements, from equilibrium, of interparticle contact axes

κ_n, k_t, k_n, k_r: Instantaneous interparticle normal, tangential, torsional, and rolling stiffnesses

β, β_r: The instantaneous ratios of viscosity to stiffness, for normal, tangential, or torsional motion, and for rolling

μ, μ_n, μ_r: The coefficients of interparticle tangential, torsional, and rolling friction

$\mathbf{F}_n, \mathbf{F}_t$: Normal and tangential interparticle forces

$\mathbf{M}_t, \mathbf{M}_n, \mathbf{M}_r$: Interparticle torques from tangential force, torsion, and rolling resistance

e: An interparticle collision's coefficient of restitution

$V_j, \mathbf{x}_j, \mathbf{u}_j$: Particle j's volume, position, and velocity

$\mathbf{x}_j^c, \dot{\delta}_{n,j}, \dot{\delta}_{t,j}$: The location of interparticle collision j and its normal and tangential impact velocities

C, ι_C: The set of particles connected to the base by a chain of contacts, and its indicator function

$\mathbf{F} = (F_x, F_y, F_z)$: Force exerted by the flow on its base

w_z: A weight function centered on base-normal height z

$\phi(z), \mathbf{u}(z), T(z)$: The w_z-weighted mean flow volume fraction, velocity, and granular temperature

$n_I(z), \langle\dot{\delta}_n^2\rangle(z), \langle\dot{\delta}_t^2\rangle(z)$: The number of interparticle impacts per unit volume and time, and their mean squared normal and tangential impact velocities (all weighted by w_z)

$\mathcal{P}_c(z)$: The w_z-weighted proportion of particles that are connected to the base by a chain of contacts

$P_{F_\cdot}$: The power spectrum of basal force component $F_\cdot$

$\langle\mathbf{F}\rangle, p, h$: Mean basal force and pressure, and flow depth

$\bar{\phi}, \bar{u}$: Depth-averaged volume fraction and downslope velocity within the flow

u_x': The base-normal gradient of downslope velocity u_x

$\langle P_{F_\cdot}\rangle_{\Delta f}$: The moving average of power spectrum $P_{F_\cdot}$ over frequency range Δf

P_F^0, f_c: The low-frequency magnitude and corner frequency of power spectrum P_{F_z}'s high-frequency component

$\hat{\cdot}$: Model prediction for $\cdot$

ϵ: Geometric standard error in the prediction of P_F^0

g_T: A proposed constant linking shear within a flow to its granular temperature

λ: The typical base-normal extent of force chains within the flow, in units d, inferred by fitting an exponential to $\mathcal{P}_c$

J: The mean base-normal impulse transferred by a velocity-$\sqrt{\langle\dot{\delta}^2\rangle}$ interparticle collision

$\tau(\dot{\delta}_n), F_I(t)$: The timescale of, and normal force during, a Hertzian interparticle collision at normal velocity $\dot{\delta}_n$

$\zeta(\mathfrak{f})$: A non-dimensional function of non-dimensional frequency $\mathfrak{f} = f\tau$, proportional to spectral density $|\tilde{F}_I(f)|^2$

$\mathfrak{f}_c$: The value 0.200, beyond which $\zeta(\mathfrak{f})$ drops off rapidly

K: An unspecified prefactor in the model of Kean et al. (2015)

u_b, υ: The mean and relative standard deviation of basal particle velocities

χ, ξ: A shape factor for the downslope velocity profile and a non-dimensional function of υ, in the model of Farin, Tsai, Lamb, and Allstadt (2019)

γ: A constant of acoustic wave attenuation, in the model of Bachelet et al.

ι_j, η: An indicator variable for transmission of interparticle collision j's force to the flow base, and the typical fraction of its spectral power transmitted a base-normal distance d, in the minimal model.

$\mathcal{I}, \mathcal{I}_{\hat{n}}, \mathcal{I}_{\hat{P}_c}, \mathcal{I}_{\hat{T}}, \mathcal{I}_{\hat{\psi}\hat{V}}$: An integrand expressing contributions from different base-normal positions to the minimal model's $\hat{P}_F$, and its successive approximants

$\hat{V}, \hat{\psi}$: Representative values, in the parametrization of the minimal model, of interparticle impact velocity and the proportion of overburden stress transmitted via impacts to the base.

C, a, b: Parameters in the log-linear model for $(\hat{\psi}\hat{V})(h, \bar{u})$

$\hat{I}$: The bulk inertial number

$\delta\mathcal{F}^2$: The squared magnitude ratio of high-frequency force fluctuations to mean forces

S2. Unimportance of plastic yield

To examine the importance of plastic yield in particles' normal deformation, we first calculate the yield threshold necessary, in a Thornton model of normal elasto-plastic deformation (Thornton, 1997), to match Foerster, Louge, Chang, and Allia (1994)'s experimental measurements of the coefficient of restitution in collisions of glass spheres. We then examine the implications of this threshold for the interparticle collisions we wish to model.

For colliding spheres with masses m, radii r, centre-to-centre separation $2r - \delta_n$, and interparticle normal force magnitude F_n, the Thornton model at first agrees with that of Hertz (1881), with $F_n = E^*\sqrt{r\delta_n^3}$ for material-parameter-dependent E^*. But the material is supposed to have a yield stress σ_y: if δ_n increases beyond a threshold $\delta_y = (\pi\sigma_y/3E^*)^2 r$, the Thornton model instead sets $F_n = E^*\sqrt{r\delta_y}(3\delta_n - \delta_y)/2$, such that F_n is continuously differentiable with respect to δ_n but not smooth. And in this case, F_n displays hysteresis after attaining its maximum $F_{\max}$ at $\delta_{\max}$, with $F_n = E^*\sqrt{r(\delta_n - \delta_0)^3}$ until the collision ends at $\delta_n = \delta_0$, for $\delta_0 = \delta_{\max} - \sqrt[3]{F_{\max}^2/E^{*2}r}$. Collisions for which δ_y always exceeds δ_n are Hertzian and perfectly elastic. But, for lower δ_y, the work done as δ_n increases exceeds the work done as δ_n decreases, so that the coefficient of restitution is below 1.

To identify the yield threshold δ_y^* replicating Foerster et al. (1994)'s measurements, a coefficient of restitution $e_F = 0.97$ at impact velocity $v_F = 1.2\,\mathrm{m\,s^{-1}}$, we simulate this model with units that normalize both v_F and acceleration coefficient $E^*\sqrt{r}/m$: $\hat{\delta}(r) = (m^2 v_F^4/E^{*2}r)^{1/5}$ for distance and $\tau = (m^2/E^{*2}rv_F)^{1/5}$ for time. Using SciPy (Virtanen et al., 2020) within the code of Arran, Mangeney, De Rosny, and Toussaint (2023), we determine that $\delta_y^*/\hat{\delta} = 0.784$. Figure S1a illustrates the associated evolution of δ_n and F_n.

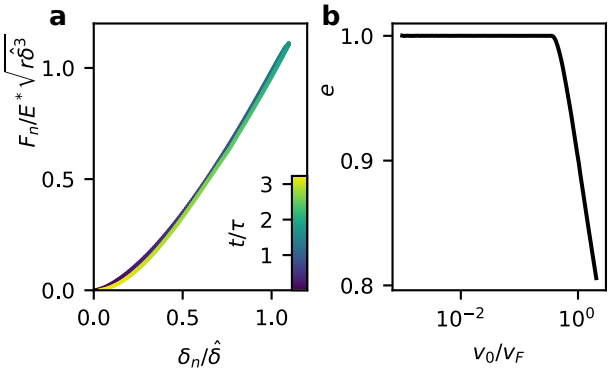

Figure S1. *Effect of plastic yield on a binary collision.* a) Normalized evolution of penetration distance δ_n and force F_n over time t, for yield threshold δ_y^* such that the coefficient of restitution is $e_F = 0.97$. b) Coefficient of restitution e as a function of impact velocity v_0, defined relative to v_F such that $e(v_F) = e_F$.

Such simulations apply directly to the particles we wish to consider. We model soda lime glass similar to that of Foerster et al. (1994), so take E^*, σ_y, and m/r^3 to be identical. Consequently, provided that units are defined using the velocity v_F, both δ_y and $\hat{\delta}$ are proportional to r. So even though our simulated particles have radii of approximately 1 mm, while the radii of Foerster et al. (1994)'s particles are 1.5 mm, the appropriate normalized yield threshold remains $\delta_y^*/\hat{\delta} = 0.784$.

Figure S1b indicates the effect of this yield threshold on collisions with varying impact velocity. For simulated impact velocities v_0 greater than $0.6v_F = 0.7\,\mathrm{m\,s^{-1}}$, the coefficient of restitution decreases with v_0, but plastic deformation along a contact's normal has no effect on the dynamics of lower-velocity collisions. Since we expect the highest impact velocities to be of order $\sqrt{2gr} = 0.14\,\mathrm{m\,s^{-1}}$ for gravitational acceleration g (as we observe in the main text's Figure 3k), we neglect particle plasticity entirely.

S3. Interparticle interactions

We describe the simulated interactions between two particles with radii r_1 and r_2, centres at $\mathbf{x}_1$ and $\mathbf{x}_2$, and velocities $\mathbf{v}_1$ and $\mathbf{v}_2$. These interact when they satisfy the contact condition

$$\delta_n = r_1 + r_2 - ||\mathbf{x}_1 - \mathbf{x}_2|| \geq 0, \tag{1}$$

with the first particle's outward unit normal to the contact

$$\hat{\mathbf{n}} = (\mathbf{x}_2 - \mathbf{x}_1)/||\mathbf{x}_2 - \mathbf{x}_1||, \tag{2}$$

and the effective radius for the interaction

$$r = \left(\frac{1}{r_1} + \frac{1}{r_2}\right)^{-1}. \tag{3}$$

Material parameters are the Young's modulus E, the Poisson ratio ν, and the shear modulus $G = E/2(1+\nu)$.

S3.1. Normal force $\mathbf{F_n}$

We first describe the normal force between two interacting particles, which depends on the rate of normal deformation

$$\dot{\delta}_n = (\mathbf{v}_1 - \mathbf{v}_2)\cdot\hat{\mathbf{n}}. \tag{4}$$

At each timestep of this contact, for the damping parameter β whose calibration is described in section S4.1, the normal force of the first particle on the second is specified to be

$$\mathbf{F}_n = \frac{2E}{3(1-\nu^2)}\sqrt{r\delta_n}(\delta_n + \beta\dot{\delta}_n)\hat{\mathbf{n}}. \tag{5}$$

This force is taken to act on a point directly between $\mathbf{x}_1$ and $\mathbf{x}_2$, and so is associated with no torque about the second particle's centre.

S3.2. Tangential force $\mathbf{F_t}$

The tangential force also has viscous and elastic components, but with the elastic force dependent on the history of loading and with the total force limited by Coulomb friction, so that the calculation of the tangential force must be performed algorithmically. Specifically, the elastic tangential force is set to be $\mathbf{F}_{te} = \mathbf{0}$ at the start of each contact and, at each timestep during the contact, four steps are performed. First, this force is adjusted to account for the rotation of the particle contact plane with respect to an inertial frame, so that, writing Δt for the time step and $\cdot^n$ for the value of a given variable at the nth timestep,

$$\mathbf{F}_{te}^n = \mathbf{F}_{te}^{n-1} - \frac{\mathbf{F}_{te}^{n-1}\cdot(\mathbf{v}_2^{n-1} - \mathbf{v}_1^{n-1})}{||\mathbf{x}_2^n - \mathbf{x}_1^n||}\Delta t\,\hat{\mathbf{n}}^n. \tag{6}$$

Next, the instantaneous tangential stiffness is set to be

$$k_t = \frac{4G}{2-\nu}\sqrt{r\delta_n}, \tag{7}$$

and the elastic force is set to its value in the case of zero tangential slip. If the particles' angular velocities are ω_1 and

ω_2, then the relative tangential velocity across the contact is

$$\dot{\delta}_t = \mathbf{v}_1 - \mathbf{v}_2 + \dot{\delta}_n\hat{\mathbf{n}} + (r_1\omega_1 + r_2\omega_2) \times \hat{\mathbf{n}}, \tag{8}$$

and so, accounting for the possibility of unloading, the updated elastic tangential force is

$$\mathbf{F}_{te}^n = \begin{cases} \mathbf{F}_{te}^{n-1} + k_t^n \Delta t\, \dot{\delta}_t & \text{if} \quad ||\mathbf{F}_n^n|| \geq ||\mathbf{F}_n^{n-1}|| \\ \frac{k_t^n}{k_t^{n-1}}\mathbf{F}_{te}^{n-1} + k_t^n \Delta t\, \dot{\delta}_t & \text{otherwise.} \end{cases} \tag{9}$$

Then, the implied tangential force, including viscous resistance, is tested against a Coulomb friction condition, with friction coefficient μ_t calibrated as decribed in section S4.3. Specifically, defining for the same damping parameter β as above,

$$\mathbf{F}_{t-ns} = \mathbf{F}_{te}^n + \beta k_t \dot{\delta}_t, \tag{10}$$

and, for $\hat{\mathbf{F}}_{t-ns} = \mathbf{F}_{t-ns}/||\mathbf{F}_{t-ns}||$, we set the tangential force of the first particle on the second to be

$$\mathbf{F}_t = \begin{cases} \mathbf{F}_{t-ns} & \text{if} \quad ||\mathbf{F}_{t-ns}|| \leq \mu_t ||\mathbf{F}_n|| \\ \mu_t ||\mathbf{F}_n|| \hat{\mathbf{F}}_{t-ns} & \text{otherwise.} \end{cases} \tag{11}$$

Finally, in the second case, where tangential slip occurs between the two particles, the elastic component of the tangential force is updated accordingly, as

$$\mathbf{F}_{te} = \mathbf{F}_t - \beta k_t \dot{\delta}_t. \tag{12}$$

The tangential force of the first particle on the second is taken to apply a torque about the latter's centre of

$$\mathbf{M}_t = (r_2 - \delta_n/2)\mathbf{F}_t \times \hat{\mathbf{n}}, \tag{13}$$

corresponding to the case of symmetric normal deformation.

S3.3. Torsional resistance $\mathbf{M_n}$

The torsional torque exerted by the first particle about the second's centre is calculated analogously to the tangential force, except as a scalar multiple of the contact normal $\hat{\mathbf{n}}$ and with different parameter values. Consequently, at the start of the contact, the elastic scalar torque is set to be $M_{ne} = 0$, and M_{ne} need not be updated to account for frame rotation. The contact stiffness is

$$k_n = \frac{16G}{3} r^{3/2} \delta_n^{3/2}, \tag{14}$$

and the scalar relative torsional rotation rate is

$$\dot{\theta}_n = (\omega_1 - \omega_2) \cdot \hat{\mathbf{n}}, \tag{15}$$

so, at the nth timestep, the elastic scalar torsional torque, in the case of zero torsional slip, is

$$M_{ne}^n = \begin{cases} M_{ne}^{n-1} + k_n^n \dot{\theta}_n \Delta t & \text{if} \quad ||\mathbf{F}_n^n|| \geq ||\mathbf{F}_n^{n-1}|| \\ \frac{k_n^n}{k_n^{n-1}} M_{ne}^{n-1} + k_n^n \dot{\theta}_n \Delta t & \text{otherwise.} \end{cases} \tag{16}$$

We impose at the Hertzian contact radius an effective Coulomb friction coefficient $\mu_n = 3\pi\mu_t/16$, so defining

$$M_{n-ns} = M_{ne} + \beta k_n \dot{\theta}_n, \tag{17}$$

we set the torsional vector torque of the first particle on the second to be

$$\mathbf{M}_n = \begin{cases} M_{n-ns}\hat{\mathbf{n}} & \text{if} \quad |M_{n-ns}| \leq \mu_n ||\mathbf{F}_n|| \sqrt{r\delta_n} \\ \mu_n ||\mathbf{F}_n|| \sqrt{r\delta_n} \text{sgn}(M_{n-ns})\hat{\mathbf{n}} & \text{otherwise,} \end{cases} \tag{18}$$

unassociated with any net force between the particles. For consistency, the elastic scalar torsional torque is updated in the second case, as

$$M_{ne} = \mathbf{M}_n \cdot \hat{\mathbf{n}} - \beta k_n \dot{\theta}_n. \tag{19}$$

S3.4. Rolling resistance $\mathbf{M_r}$

The torque imposed by rolling resistance is also calculated in a manner analagous to the tangential force. Again, the elastic component of the rolling resistance torque is initialized at the start of the contact, by setting $\mathbf{M}_{re} = 0$, and updated at each timestep to account for frame rotation, by setting

$$\mathbf{M}_{re}^n = \mathbf{M}_{re}^{n-1} - \frac{\mathbf{M}_{re}^{n-1} \cdot (\mathbf{v}_2^{n-1} - \mathbf{v}_1^{n-1})}{||\mathbf{x}_2^n - \mathbf{x}_1^n||} \Delta t\, \hat{\mathbf{n}}^n. \tag{20}$$

The rate of rolling is

$$\dot{\theta}_r = \omega_1 - \omega_2 - [(\omega_1 - \omega_2) \cdot \hat{\mathbf{n}}]\hat{\mathbf{n}} \tag{21}$$

and the stiffness is, for constant κ discussed in section S4.2,

$$k_r = 2\kappa ||\mathbf{F}_n|| r, \tag{22}$$

so the elastic component of the torque resisting rolling is, at the nth time step and in the case of zero slip,

$$\mathbf{M}_{re}^n = \begin{cases} \mathbf{M}_{re}^{n-1} + k_r^n \dot{\theta}_r \Delta t & \text{if} \quad ||\mathbf{F}_n^n|| \geq ||\mathbf{F}_n^{n-1}|| \\ \frac{k_r^n}{k_r^{n-1}} \mathbf{M}_{re}^{n-1} + k_r^n \dot{\theta}_r \Delta t & \text{otherwise.} \end{cases} \tag{23}$$

For the rolling damping parameter β_r and rolling friction coefficient μ_r discussed in section S4.2, we define

$$\mathbf{M}_{r-ns} = \mathbf{M}_{re} + \beta_r k_r \dot{\theta}_r \tag{24}$$

and $\hat{\mathbf{M}}_{r-ns} = \mathbf{M}_{r-ns}/||\mathbf{M}_{r-ns}||$, and set the torque imposed by rolling resistance to be

$$\mathbf{M}_r = \begin{cases} \mathbf{M}_{r-ns} & \text{if} \quad ||\mathbf{M}_{r-ns}|| \leq \mu_r ||\mathbf{F}_n|| r \\ \mu_r ||\mathbf{F}_n|| r \hat{\mathbf{M}}_{r-ns} & \text{otherwise.} \end{cases} \tag{25}$$

Again, the torque is not associated with any net force and is updated in the second case, as

$$\mathbf{M}_{re} = \mathbf{M}_{r-ns} - \beta_r k_r \dot{\theta}_r. \tag{26}$$

S4. Parameter selection

In implementing the interparticle interactions described in section 3, we use non-dimensionalizations of the dimensional parameter values listed in Table S1. The following subsections describe the selection of those values not derived from material databases or other parameter values, with section S4.1 describing the selection of the damping parameter β; section S4.2 that of rolling resistance parameters κ, β_r, and μ_r; section S4.3 that of the tangential friction coefficient μ_t; S4.4 that of modified parameters to model interactions with a PMMA channel wall and a plane of symmetry; and section S4.5 that of the simulation timestep δt.

Table S1. *Simulation parameter values.* For each parameter, we list its name, symbol, and dimensional value, and the source for this value. 'A21' and 'SV05' indicate Arran et al. (2021) and Seward and Vascott (2005). 'Der.' indicates derived values $G = E/2(1+\nu)$, $\mu_n = 3\pi\mu_t/16$, and $G_w = E_w/2(1+\nu_w)$. Other sources are subsections of this supporting information, describing parameter selection.

Parameter	·	Value	Source
Particle radius	r	(1.00 ± 0.05) mm	A21
Density	ρ	$2530\,\mathrm{kg/m^3}$	SV05
Young's modulus	E	74 GPa	SV05
Poisson's ratio	ν	0.22	SV05
Shear modulus	G	30 GPa	Der.
Damping parameter	β	45.1 ns	S4.1
Tangential friction coefficient	μ_t	0.237	S4.3
Torsional friction coefficient	μ_n	0.140	Der.
Rolling stiffness modulus	κ	0.742	S4.2
Rolling damping parameter	β_r	2.0 ms	S4.2
Rolling friction coefficient	μ_r	0.0175	S4.2
Sidewall Young's modulus	E_w	3.3 MPa	S4.4
Sidewall Poisson's ratio	ν_w	0.4	S4.4
Sidewall shear modulus	G_w	1.18 MPa	Der.
Sidewall damping parameter	β_w	200 ns	S4.4
Sidewall friction coefficient	μ_w	0.105	S4.4
Timestep	δt	2.5×10^{-7} s	S4.5

velocity on a) contact time and b) effective restitution coefficient are shown in Figure S2.

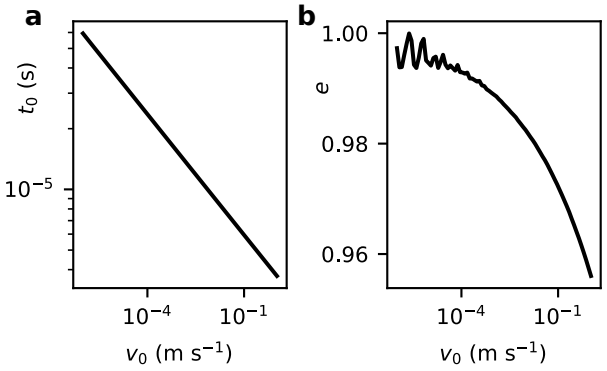

Figure S2. *Effect of viscous damping on a binary collision.* Simulated collision duration t_0 (a) and coefficient of restitution e (b) as functions of impact velocity v_0, for simulated damping parameter $\beta^* = 45.1$ ns consistent with Foerster et al. (1994).

S4.1. Damping parameter β

Since the damping parameter β is difficult to measure directly, we seek to calibrate its value using measurements of the coefficient of restitution. Noting that β is a function only of material parameters and has dimensions of time, we take its value from Foerster et al. (1994)'s experiments on binary collisions of ($2r_F = 3$ mm)-diameter soda lime glass spheres ($\rho_F = 2500\,\mathrm{kg/m^3}$, $E_F = 71$ MPa, $\nu_F = 0.22$), similar to those of Arran et al. (2021)'s experiments. At normal incidence velocities up to $v_F = 1.2\,\mathrm{m\,s^{-1}}$, the coefficient of restitution was 0.97 ± 0.01.

We proceed analogously to section S2: first non-dimensionalizing the collision's evolution equations with distance $\hat{\delta}_F = (\pi\rho_F(1-\nu_F^2)v_F^2/4E_F)^{2/5}r_F$ and time $\tau_F = \hat{\delta}_F/v_F$, then simulating collisions for varying non-dimensional damping parameters β/τ_F to identify the value $\beta^*/\tau_F = 0.0265$ for which the coefficient of restitution is 0.97, and finally applying to our simulations the dimensional damping parameter $\beta^* = 45.1$ ns appropriate to Foerster et al. (1994)'s experiments. The consequent effects of incidence

S4.2. Rolling resistance parameters κ, β_r, μ_r

We use experiments on single particles to select values for the non-dimensional rolling stiffness modulus κ, the rolling damping parameter β_r, and the rolling friction coefficient μ_r. Since rolling resistance arises primarily from the particles' deviations from sphericity, the rolling resistance of a radius r particle on a stiff, flat plane will be approximately the same as that between two particles with harmonic mean radius r.

In the first experiment, each of 9 randomly selected particles is, in turn, placed on a flat metal plate. The plate is accelerated and brought to a rapid stop, at which point the particle's inertia and the friction at its contact point cause it to roll. Rolling resistance slows the particle's rotation until it reaches the no-slip regime described above, at which point it displays exponentially decaying harmonic oscillations about a local, stable equilibrium. Filming these oscillations at 250 frames per second, with an Optronis CR600x2 high-speed camera with Sigma 17-50 mm F2.8 EX DC lense, we use cross-correlation between successive images to extract the particle's horizontal velocity u. Under the no-slip viscoelastic model for rolling resistance described in section S3.4, this velocity satisfies, for some constants u_0 and ϕ_0 and for I equal to the particle's moment of inertia,

$$u = u_0 \sin\left(\phi_0 + t\sqrt{\frac{k_r}{I} + \frac{\beta_r^2 k_r^2}{4I^2}}\right)\exp\left(-\frac{\beta_r k_r}{2I}t\right). \quad (27)$$

Therefore, fitting a relation of this form to the decaying oscillations, minimizing the sum of squared residuals, and noting that the particle is an approximate sphere under gravity, so that $k_r/I = 5\kappa g/2r$, we calculate the κ and β_r consistent with the particle's motion. Averaging these over the 9 repeats with different particles, we recover the values

$$\kappa = 0.742, \qquad \beta_r = 0.0020\,\mathrm{s}. \quad (28)$$

To illustrate this workflow, Figure S3 presents its application to an orange of circumference 28 cm, using an updated version of the code.

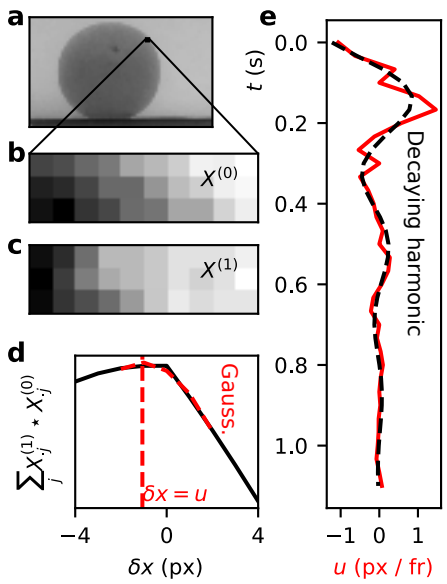

Figure S3. *Calibration of rolling resistance parameters.* From the first frame of a movie of a rolling orange (a), we compare an enlargement of the row-mean-subtracted intensity matrix $X^{(0)}$ (b) with the equivalent for the next frame's equivalent $X^{(1)}$ (c). d) Calculating the sum of row-wise convolutions at small shifts δx and fitting a Gaussian in the vicinity of the maximum recovers the horizontal velocity u at sub-pixel resolution. e) Fitting a decaying harmonic oscillation to the time-t evolution of u recovers the parameters for rolling resistance.

In the second experiment, we repeatedly place a particle at the top of a $L = 20$-cm long glass plate, inclined at an angle Θ, and disturb the particle's position until it starts to roll. We then record whether it continues rolling until it reaches the bottom of the plate. By varying the plate's inclination between trials, we find:

1. the maximum angle $\Theta_M = 0.9°$ at which the bottom is reached on none of five successive attempts, and

2. the minimum angle $\Theta_m = 1.1°$ at which the bottom is reached on all of five successive attempts.

Using the model for rolling resistance described above and writing m for the particle's mass, its angular acceleration while freely rolling will be

$$\ddot{\theta} = \frac{mgr}{I} \cos\Theta(\tan\Theta - \mu_r), \tag{29}$$

so that the particle will reach the bottom of the plate if and only if

$$\mu_r \leq \tan\Theta + \frac{I\omega_0^2}{mgL\cos\Theta}, \tag{30}$$

for ω_0 the particle's initial angular velocity, of order $10\,\mathrm{s}^{-1}$. With the latter term of order 10^{-5}, and so negligible, we estimate μ_r as the average of its upper and lower bounds $\tan\Theta_M$ and $\tan\Theta_m$, recovering

$$\mu_r = 0.0175. \tag{31}$$

S4.3. Sliding friction coefficient μ_t

Having selected all other interaction parameters, we select the value of the microscopic sliding friction μ_t for which the angle of repose in simulations matches an experimentally measured value for glass beads.

Experimentally, we half fill a tray with glass beads, vibrating the tray to ensure the bead pack's surface is level. We then incline the tray until the beads avalanche, wait until the avalanching beads come to rest, and increase its inclination again until another avalanche occurs. By measuring these two changes in the bead pack's surface's inclination, from 0° up to the beads' avalanche angle θ_a, and from their angle of repose θ_r up to their avalanche angle θ_a, we calculate an estimate of the angle of repose θ_r. Repeating the experiment 12 times and averaging the estimates, we recover $\theta_r = 21.9 \pm 0.6°$.

To match simulations to experiments, we conduct a binary search to find the lowest sliding friction coefficient for which simulated beads come to a rest with a surface angle of $\theta_r = 21.9°$. Specifically, we start with $\mu_t^- = 0$ and $\mu_t^+ = 1$ as bounds for the 'true' value of the sliding friction coefficient and select a trial value $\mu_t^0 = (\mu_t^- + \mu_t^+)/2$, with which we run a simulation according to the protocol described in section 2.1, with $n_x = n_y = n_z = 10$ and with $\theta = 21.9°$. We use a timestep equivalent to 2.5×10^{-7} s, so that there are 200 timesteps during a simulated binary collision at velocity $\sqrt{gd} = 0.14\,\mathrm{m\,s}^{-1}$ (see Figure S2a). If the simulation attains a steady, non-static state, then this friction coefficient is insufficiently large for the simulated beads to match experiments and we update μ_t^- to μ_t^0. If the simulated beads come to a rest, we update μ_t^+ to μ_t^0. Either way, we continue the procedure until the bounds constrain the 'true' value to three significant figures and we use this 3 s.f. value for μ_t. We recover

$$\mu_t = 0.237. \tag{32}$$

S4.4. Channel boundary parameters $\cdot_w$

To consider the effect of lateral boundaries, we run simulations in which there is a fixed wall at $y = 0$, corresponding to an acrylic (PMMA) channel wall, and another at $y = 50d$, corresponding to a symmetry condition at the midline of a channel. We illustrate this in Figure S4. Interactions between particles and the walls are modelled in the same way as those between particles, as described in section S3, except with appropriately changed definitions and values of material parameters.

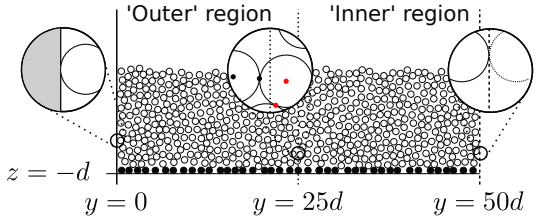

Figure S4. *Schematic of simulated channel flow.* Compared to the doubly periodic domain, we simulate a PMMA wall (solid line at left) and a plane of symmetry (dashed line at right), including during preparation of the fixed basal particles (black), and we restrict the coarse-graining described in section S5 to the half of the flow away from the wall (right of the dotted line at center). Detail views demonstrate, from left to right: particles' effective interaction with the PMMA wall (gray); selection of particles and contacts to include in coarse-graining (marked red, rather than black); and particles' interaction with the plane of symmetry, at which any particle is effectively confronted with a mirrored copy (dotted part circle).

Specifically, in place of condition (1), we take a particle with radius r_2 and y-co-ordinate y_2 to be in contact

and hence interacting with the wall at $y = 0$ if overlap $\delta_n = r_2 - y_2 \geq 0$. For such a wall-particle interaction, we use a 'first particle' velocity $\mathbf{v}_1 = \mathbf{0}$ and a 'first particle' angular velocity $\omega_1 = \mathbf{0}$, while redefining the outwards normal of equation (2) as $\hat{\mathbf{n}} = \mathbf{e}_y$; the effective radius of equation (3) as $r = r_2$; and the inverse separation $||\mathbf{x}_2 - \mathbf{x}_1||^{-1}$ as 0 in equations (6) and (20). Taking the Young's modulus of PMMA to be $E_w = 3.3$ MPa, its Poisson ratio to be $\nu_w = 0.4$, and its shear modulus to be $G_w = E_w/2(1+\nu_w)$, we replace the values $E/(1-\nu^2)$ in equation (5), $G/(1-\nu)$ in equation (7), and G in equation (14) with their corresponding harmonic means

$$2\left(\cdot^{-1} + \cdot_w^{-1}\right)^{-1}. \tag{33}$$

The sliding friction coefficient μ_w between a glass particle and the PMMA wall is taken to correspond to the 6° minimum angle at which a plate coated with glued glass beads slides on a PMMA plate, such that $\mu_w = 0.105$, and this value replaces μ_t in equations (11) and (18). Finally, the damping parameter β_w for a collision between a glass particle and the PMMA wall is taken to be that necessary for a glass bead dropped onto a PMMA plate from a height of $h = 0.1$ m to have a rebound height of 0.08 m, such that $\beta_w = 2 \times 10^{-7}$ s, and this value replaces β in equations (5), (10), (12), (17), and (19).

Correspondingly, we take a particle with radius r_2 and y-co-ordinate y_2 to be in contact with the wall at $y = 50d$ if overlap $\delta_n = r_2 - (50d - y_2) > 0$. For interactions between this wall and the particle, we use an outwards normal $\hat{\mathbf{n}} = -\mathbf{e}_y$, but again take an effective radius $r = r_2$, an inverse separation $||\mathbf{x}_2 - \mathbf{x}_1||^{-1} = 0$, a 'first particle' velocity $\mathbf{v}_1 = \mathbf{0}$, and a 'first particle' angular velocity $\omega_1 = \mathbf{0}$. We want the interaction of a particle with the wall to be equivalent to that of the particle with an identical particle, exactly reflected in the plane $y = 50d$, but note that r has twice the value it would have in that case and δ_n half the value it would have. We therefore we use in equation (5) a value of $E/(1-\nu^2)$ that is twice that used for interparticle collisions, ensuring that $\mathbf{F}_n$ takes the exact value it would have in an interparticle interaction with a reflected particle. Similarly, we note that a particle would experience no tangential motion or torsional rotation relative to its exact reflection, and so set the tangential force and torsional torque to zero by replacing μ_t with zero in equations (11) and (18). Finally, since $\omega_1 = 0$ rather than $-\omega_2$ and $r = r_2$ rather than $r_2/2$, $\dot{\theta}_r$ is defined to be half the value it would in the case of an interaction with a reflected particle while k_r has a value twice as large, and so equations (23), (24) and (26) need not be changed to ensure a correct value of rolling resistance.

S4.5. Timestep δt

We wish to verify that a timestep $\delta t = 2.5 \times 10^{-7}$ s is sufficiently small that, even for a collision with atypically high normal incident velocity and hence with atypically short duration, the root mean squared discretization error in the normal force is less than 1% of the root mean squared normal force. Relative errors may be larger for tangential forces and in torsional and rolling moments, which evolve in a more complex fashion during a collision, but are likely to be less significant both for a flow's properties and for the basal forces it exerts. For collisions with longer duration, discretization errors will be smaller.

To identify the extremal values of normal incident velocities, we conduct a trial steady-state simulation, according to the protocol of section 2.2 and with timestep $\delta t = 2.5 \times 10^{-7}$ s, parameter values as above, and simulated slope angle $\theta = 24.5°$, overburden $n_z = 16$, and duration $\Delta t = 0.5$ s. Over 1.8 million collisions, the 99.9th percentile of simulated normal incidence velocity was $0.362\,\mathrm{m\,s^{-1}}$.

We then use SciPy's (Virtanen et al., 2020) `solve_ivp` function to estimate the true evolution of normal force during a collision with such an impact velocity, with absolute and relative error tolerances for normalized quantities of 10^{-6}, and compare this evolution with that estimated using MercuryDPM's velocity Verlet algorithm (Weinhart et al., 2020) and various timesteps δt. The implementation of Arran et al. (2023) finds a simulation timestep of 3.4×10^{-7} s to be that for which the root mean squared discrepancy in normal force is equal to 1% of the root mean squared normal force (see Figure S5), so that $\delta t = 2.5 \times 10^{-7}$ s is sufficiently small for our purposes.

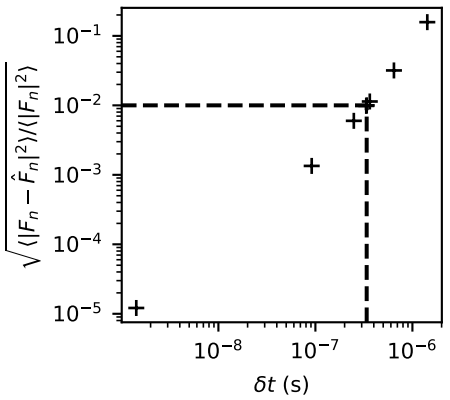

Figure S5. *Time-discretization error in simulating interparticle force during a collision at* $0.362\,\mathrm{m\,s^{-1}}$. For various timesteps δt, we calculate at each time $k\delta t$ the 'true' normal force F_n and that derived using a velocity Verlet algorithm, $\hat{F}_n$. We thereby identify the timestep 3.4×10^{-7} s for which the normalized root mean squared discrepancy is 0.01.

S5. Coarse-graining

The coarse-graining process calculates local weighted averages of the properties of discrete particles, while respecting mass and momentum conservation. In our implementation, we average over horizontal directions x and y and over all times t_k while resolving the base-normal direction z, using truncated Gaussian weight functions of width equal to the median particle diameter d:

$$w_z(\mathbf{x}_j) = \begin{cases} \frac{\exp(-2(z_j-z)^2/d^2)}{XYd\Delta t\,\mathrm{erf}(K\sqrt{2})}\sqrt{\frac{2}{\pi}} & \text{if } |z_j - z| < Kd \\ 0 & \text{otherwise,} \end{cases} \tag{34}$$

where X and Y are the downslope and cross-slope extents of the cross-graining domain, Δt is the time duration simulated, and K is a cutoff. We take X and Y to be $n_x d$ and $n_y d$ for the simulations with periodic boundaries in the cross-slope direction, and $n_x d$ and $n_y d/2$ when simulating flow in a channel. We take $K = 3$ to calculate the kinematic profiles $\phi(z)$, $\mathbf{u}(z)$ and $T(z)$, while taking K to be infinite in calculating the profiles $P_C(z)$, $n_I(z)$, $\langle\dot{\delta}_n^2\rangle(z)$ and $\langle||\dot{\boldsymbol{\delta}}_t||^2\rangle(z)$.

The kinematic profiles are defined from the timestep δt and particle positions $\mathbf{x}_j(t_k)$, volumes V_j, and velocities

$\mathbf{u}_j(t_k)$, excluding all fixed, basal particles, as

$$\phi(z) = \sum_j \sum_k w_z(\mathbf{x}_j(t_j))V_j\delta t, \tag{35}$$

$$\mathbf{u}(z) = \sum_j \sum_k w_z(\mathbf{x}_j(t_k))V_j\mathbf{u}_j(t_k)\delta t/\phi(z), \tag{36}$$

$$T(z) = \frac{1}{3}\sum_j \sum_k w_z(\mathbf{x}_j(t_k))V_j||\mathbf{u}_j(t_k) - \mathbf{u}(z)||^2\delta t/\phi(z), \tag{37}$$

while the probability profile $P_C(z)$ is defined to be

$$P_c(z) = \frac{\sum_j \sum_k w_z(\mathbf{x}_j(t_k))\iota_{C(t_k)}(j)}{\sum_j \sum_k w_z(\mathbf{x}_j(t_k))}, \tag{38}$$

where basal particles are included in the sum and $\iota_{C(t_k)}(j)$ is 1 if particle j is in the time-t_k base-connected set $C(t_k)$ and 0 otherwise. The collisional profiles are defined from each collision's contact point $\mathbf{x}_j^c$ and relative normal and tangential velocities $\dot{\delta}_{n,j}$ and $\dot{\delta}_{t,j}$, by

$$n_I(z) = \sum_j w_z(\mathbf{x}_j^c), \tag{39}$$

$$\langle\dot{\delta}_n^2\rangle(z) = \sum_j w_z(\mathbf{x}_j^c)\dot{\delta}_{n,j}^2/n_I(z), \tag{40}$$

$$\langle||\dot{\delta}_t||^2\rangle(z) = \sum_j w_z(\mathbf{x}_j^c)||\dot{\delta}_{t,j}||^2/n_I(z). \tag{41}$$

For the simulations of channel flow, all the sums above are restricted to particles with $y_j(t_k) > n_y d/2$ or to collisions with $y_j^c(t_k) > n_y d/2$. All profiles are calculated at $16n_z$ values of z, separated by intervals of $d/4$ and starting from $z = -7d/8$, just above the fixed boundary at $z = -d$.

S6. The power spectrum of Hertzian collision force

Here, we consider the spectral density $|\tilde{F}_I(f)|^2$ of the time-dependent normal force $F_I(t)$ exerted during the Hertzian impact of one spherical particle on another, extending the work of section S3 of the Supporting Information of Arran et al. (2021). As in our sections 2.3 and S3, we write ρ, d and $\dot{\delta}_n$ for the particle density, diameter and impact velocity, and E and ν for the Young's modulus and the Poisson ratio, to define timescale

$$\tau(\dot{\delta}_n) = \left[\frac{\pi^2\rho^2(1-\nu^2)^2}{4E^2\dot{\delta}_n}\right]^{1/5} d. \tag{42}$$

From Arran et al. (2021), during the impact, $F_I(t) \propto \Delta(T)^{3/2}$ for non-dimensional impact duration $T = t/\tau$ and penetration distance $\Delta(T)$, satisfying the system of equations

$$\begin{aligned}\Delta(0) &= 0,\\ \Delta'(0) &= 1,\\ \Delta''(T) &= -\Delta(T)^{3/2}.\end{aligned} \tag{43}$$

We solve this system of equations numerically, recovering the trajectory in Figure S6a and calculating the total non-dimensional impact duration: the value $T_0 = 3.22$ of T at which $\Delta(T)$ returns to zero. $\tilde{F}_I(0)$ is then the integral of $F_I(t)$ over $t \in [0, T_0\tau]$, which is equal to the impulse imparted by the perfectly elastic impact, $\pi\rho d^3\dot{\delta}_n/3$.

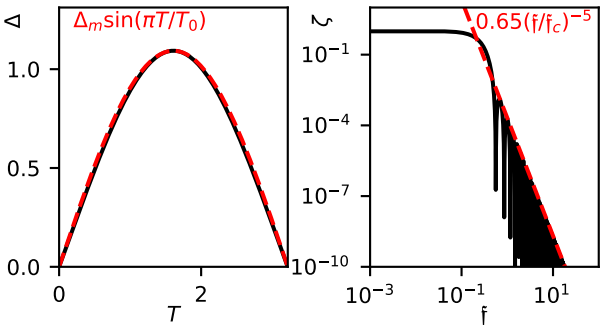

Figure S6. *Evolution of a non-dimensionalized Hertzian impact.* We compare numerical solutions (black, solid lines) and analytical approximations (red, dashed lines) of penetration distance Δ over time T and normalized power spectrum ζ over frequency $\mathfrak{f}$.

We also follow Arran et al. (2021) in numerically estimating the normalized power spectrum

$$\begin{aligned}\zeta(\mathfrak{f}) &= |\tilde{F}_I(\mathfrak{f}/\tau)|^2/|\tilde{F}_I(0)|^2\\ &= \left|\int_0^{T_0}\Delta(T)^{3/2}e^{-2\pi i\mathfrak{f}T}\,\mathrm{d}T\right|^2 \Big/ \left|\int_0^{T_0}\Delta(T)^{3/2}\right|^2.\end{aligned} \tag{44}$$

Figure S6b represents ζ, with $\zeta(0) = 1$, $\zeta \to 0$ as $\mathfrak{f} \to \infty$, $\mathfrak{f}_c = \min\{\mathfrak{f}|\zeta(2\mathfrak{f}) < \zeta(\mathfrak{f})/10\} = 0.200$, and $\zeta(\mathfrak{f}_c) = 0.529$.

In addition to this numerical solution, we calculate an approximate analytical asymptote. By comparing equations (43) to the equations of harmonic motion, we note that $\Delta(T) \approx \Delta_1(T) = \Delta_m \sin(\pi T/T_0)$, for Δ_m the maximum of $\Delta(T)$. Representing sin with exponential functions and representing the consequent binomial by its absolutely convergent expansion,

$$\begin{aligned}\sin^{3/2}(T^*) &= \left[\frac{-1}{2i}e^{-iT^*}\left(1 - e^{2iT^*}\right)\right]^{3/2}\\ &= \frac{ie^{\pi i/4}}{2\sqrt{2}}e^{-\frac{3}{2}iT^*}\left[1 - \frac{3}{2}e^{2iT^*}\right.\\ &\quad\left. + \sum_{n=2}^{\infty}\frac{1}{n!}\left(\frac{3}{2}\right)\left(\frac{1}{2}\right)\cdots\left(\frac{5}{2} - n\right)\left(-e^{2iT^*}\right)^n\right]\\ &= \frac{i-1}{4}\left[e^{-\frac{3}{2}iT^*} - \frac{3}{2}e^{\frac{1}{2}iT^*} + \sum_{n=2}^{\infty}a_n e^{\left(2n-\frac{3}{2}\right)iT^*}\right],\end{aligned} \tag{45}$$

for

$$\begin{aligned}a_n &= \frac{3}{2^n n!}\frac{(-1)^n(2n-4)!}{2^{n-2}(n-2)!}(-1)^n\\ &\approx \frac{3(2n-4)^{2n-\frac{7}{2}}e^{-(2n-4)}}{2^{2n-\frac{3}{2}}n^{n+\frac{1}{2}}(n-2)^{n-\frac{3}{2}}e^{-(2n-2)}\sqrt{\pi}} \text{ for } n > 2\\ &= \frac{3e^2}{4\sqrt{\pi}}\left(1 - \frac{2}{n}\right)^{n-2}n^{-\frac{5}{2}}\\ &\sim \frac{3}{4\sqrt{\pi}}n^{-\frac{5}{2}} \text{ as } n \to \infty.\end{aligned} \tag{46}$$

Now, the Fourier transform of the nth exponential is

$$\begin{aligned}\mathfrak{F}_n(\mathfrak{f}) &= \int_0^{T_0} e^{\left(2n-\frac{3}{2}\right)\pi i T/T_0} e^{-2\pi i \mathfrak{f} T}\ \mathrm{d}T, \\ &= \begin{cases} T_0 & \text{for } \mathfrak{f} = \frac{n-3/4}{T_0} \\ \frac{\exp\left[\left(2n-\frac{3}{2}-2\mathfrak{f}T_0\right)\pi i\right]-1}{2\mathfrak{f}T_0-2n+\frac{3}{2}} \frac{i}{\pi} T_0 & \text{otherwise,} \end{cases} \end{aligned} \tag{47}$$

vanishing at $\mathfrak{f}_k = \left(k-\frac{3}{4}\right)/T_0$ for $k \in \mathbb{N}_0/\{n\}$. Therefore,

$$\begin{aligned}\int_0^{T_0} \Delta_1(T)^{3/2} e^{-2\pi i \mathfrak{f}_k T}\ \mathrm{d}T &= \begin{cases} \frac{i-1}{4}\Delta_m^{3/2} T_0 & \text{for } k=0 \\ \frac{3(1-i)}{8}\Delta_m^{3/2} T_0 & \text{for } k=1 \\ \frac{i-1}{4} a_k \Delta_m^{3/2} T_0 & \text{for } k \geq 2 \end{cases} \\ &\sim \frac{3(i-1)}{16\sqrt{\pi}} k^{-\frac{5}{2}} \Delta_m^{3/2} T_0 \text{ as } k \to \infty, \end{aligned} \tag{48}$$

while

$$\begin{aligned}\int_0^{T_0} \Delta_1(T)^{3/2}\ \mathrm{d}T &= \frac{1}{\pi}\Delta_m^{3/2} T_0 \int_0^{\pi} \sin^{3/2}(u)\ \mathrm{d}u \\ &= \frac{2\sqrt{2}}{3\pi} K(1/2) \Delta_m^{3/2} T_0 \end{aligned} \tag{49}$$

for complete elliptic integral of the first kind K (Wolfram Alpha, 2023).

Consequently, as $\mathfrak{f}_k \to \infty$,

$$\begin{aligned}\zeta(\mathfrak{f}_k) &\approx \frac{81\pi}{1024 K(1/2)^2} (\mathfrak{f}_k T_0)^{-5} \\ &\approx 0.653 (\mathfrak{f}_k/\mathfrak{f}_c)^{-5}. \end{aligned} \tag{50}$$

Differentiating equation (47) with respect to $\mathfrak{f}$ shows that this is approximately the maximum of ζ in the interval $(k-1)/T_0 < \mathfrak{f} \leq k/T_0$, with the approximation exact in the limit $k \to \infty$, while $\Delta(T)$'s symmetry about $T_0/2$ implies that $\zeta(k/T_0) = 0$. Therefore, the central moving average over $1/T_0$ intervals is

$$\langle\zeta\rangle(\mathfrak{f}) \approx 0.33 (\mathfrak{f}_k/\mathfrak{f}_c)^{-5}. \tag{51}$$

S7. Impact geometry

We consider the geometry of an impact force's transmission through a connected network of particles, towards the flow's base, focusing on a diameter-d particle's contacts with its upper and lower neighbors. The network is likely to be structured and highly anisotropic but, for the sake of simplicity, we consider contacts in isolation and suppose a high degree of network isotropy.

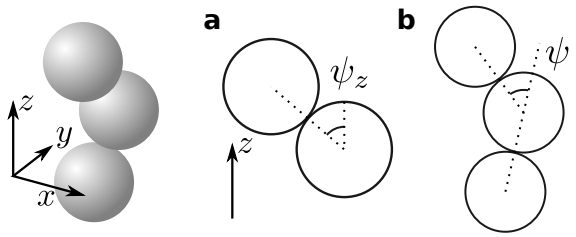

Figure S7. *Geometry of force transmission.* We illustrate the geometry of an impact force's transmission in a chain of three particles, with cross-sections a and b illustrating the base-normal distance over which the force is transmitted and the force's geometric attenuation, respectively.

If ψ_z is the angle between the upper contact's normal and the base-normal z-axis, as in Figure S7a, and the probability distribution of this contact's position depends on ψ_z only via the line element $\sin\psi_z \mathrm{d}\psi_z$, then the mean base-normal distance between the centres of the particles in contact is

$$\int_0^{\pi/2} d\cos\psi_z \sin\psi_z\ \mathrm{d}\psi_z = d/2. \tag{52}$$

Similarly, if ψ is the angle between the two contacts' normals, as in Figure S7b, then a normal force $\mathbf{F}_n$ applied at the upper contact will induce a normal force of magnitude $||\mathbf{F}_n|| \cos\psi$ at the lower contact. If the lower contact is equally likely to lie anywhere in the opposing hemisphere, then the mean fraction of spectral power transmitted will be

$$\int_0^{\pi/2} \cos^2\psi \sin\psi\ \mathrm{d}\psi = 1/3. \tag{53}$$

S8. Domain size effects

For computational tractability, we simulate flows in periodic domains much smaller than the experimental domain of Arran et al. (2021), which in turn contained many fewer particles than geophysical flows of concern. We must therefore examine whether the behavior of our simulated flows depends significantly on the domain size.

Figure S8 shows that our simulated domains are sufficiently large for there to be no systematic dependence on domain size. Holding slope angle θ and overburden n_z constant, some variation is apparent between flows in differently sized domains, both in depth profiles of downslope velocity u_x and in those of the proportion $\mathcal{P}_c$ of particles connected to the base. But whilst this variation is non-negligible, especially for $u_x(z)$-profiles of high-θ, low-n_z, highly energetic flows, no trend with domain size A can be discerned. The variation can therefore be attributed to random influences, such as details of base preparation or of initial conditions.

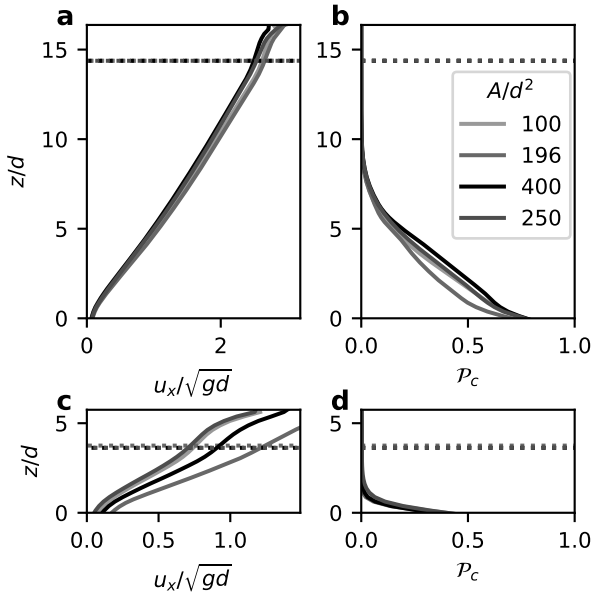

Figure S8. *Variation with domain size.* Profiles with base-normal coordinate z of (a, c) downslope velocity u_x and (b, d) the probability $\mathcal{P}_c$ that a particle is connected to the base, for various domain sizes A and for (a, b) $\theta = 22.0^\circ$ and $n_z = 16$ and (c,d) $\theta = 24.5^\circ$ and $n_z = 4$.

Movie S1.
Illustration of simulated steady flow, for domain extents $n_x = n_y = 10$, slope angle $\theta = 23.5^\circ$ and overburden $n_z = 11$. Particles are represented by spheres of corresponding diameter, with fixed basal particles black and other particles colored according to their simulated velocity, in $\mathrm{m\,s^{-1}}$. Consecutive frames are separated by 0.001 simulated seconds, so that the video spans 0.32 s of simulated flow, starting 4 s before the time t_0 at which the flow is flow is confirmed to be steady.

Movie S2.
Illustration of force chains within a simulated flow, for domain extents $n_x = n_y = 10$, slope angle $\theta = 22.0^\circ$ and overburden $n_z = 8$. In the jth frame, corresponding to time $t_0 + j\delta t$, each pair of particles in contact is indicated by a line segment joining their centres, with opacity and color corresponding to the interparticle normal force F_n.

Movie S3.
As for Movie S2, but with slope angle $\theta = 24.5^\circ$ and overburden $n_z = 8$, and with F_n frequently exceeding the saturation value $400\rho g d^3$.

References

Arran, M. I., Mangeney, A., De Rosny, J., Farin, M., Toussaint, R., & Roche, O. (2021). Laboratory landquakes: Insights from experiments into the high-frequency seismic signal generated by geophysical granular flows. *Journal of Geophysical Research: Earth Surface*, *126*(5), e2021JF006172. Retrieved from `https://agupubs.onlinelibrary.wiley.com/doi/abs/10.1029/2021JF006172` (e2021JF006172 2021JF006172) doi: 10.1029/2021JF006172

Arran, M. I., Mangeney, A., De Rosny, J., & Toussaint, R. (2023). *Simulated Slidequakes, v1.0.* Zenodo. doi: 10.5281/zenodo.8219510

Farin, M., Tsai, V. C., Lamb, M. P., & Allstadt, K. E. (2019). A physical model of the high-frequency seismic signal generated by debris flows. *Earth Surface Processes and Landforms*, *44*(13), 2529–2543. Retrieved from `https://onlinelibrary.wiley.com/doi/abs/10.1002/esp.4677` doi: 10.1002/esp.4677

Foerster, S. F., Louge, M. Y., Chang, H., & Allia, K. (1994). Measurements of the collision properties of small spheres. *Physics of Fluids*, *6*(3), 1108–1115. Retrieved from `https://doi.org/10.1063/1.868282` doi: 10.1063/1.868282

Hertz, H. R. (1881). Über die berührung fester elastischer körper. *Journal für die reine und angewandte Mathematik*, *92*, 156–171. Retrieved from `https://home.uni-leipzig.de/pwm/web/download/Hertz1881.pdf`

Kean, J. W., Coe, J. A., Coviello, V., Smith, J. B., McCoy, S. W., & Arattano, M. (2015). Estimating rates of debris flow entrainment from ground vibrations. *Geophysical Research Letters*, *42*(15), 6365–6372. Retrieved from `https://agupubs.onlinelibrary.wiley.com/doi/abs/10.1002/2015GL064811` doi: 10.1002/2015GL064811

Seward, T. P., III, & Vascott, T. (Eds.). (2005). *High temperature glass melt property database for process modeling.* The American Ceramic Society.

Thornton, C. (1997, 06). Coefficient of restitution for collinear collisions of elastic-perfectly plastic spheres. *Journal of Applied Mechanics*, *64*(2), 383–386. Retrieved from `https://appliedmechanics.asmedigitalcollection.asme.org/article.aspx?articleid=1412715` doi: 10.1115/1.2787319

Virtanen, P., Gommers, R., Oliphant, T. E., Haberland, M., Reddy, T., Cournapeau, D., ... SciPy 1.0 Contributors (2020). SciPy 1.0: Fundamental Algorithms for Scientific Computing in Python. *Nature Methods*, *17*, 261–272. doi: 10.1038/s41592-019-0686-2

Weinhart, T., Orefice, L., Post, M., van Schrojenstein Lantman, M. P., Denissen, I. F., Tunuguntla, D. R., ... Thornton, A. R. (2020). Fast, flexible particle simulations — an introduction to mercurydpm. *Computer Physics Communications*, *249*, 107129. Retrieved from `https://www.sciencedirect.com/science/article/pii/S0010465519304357` doi: 10.1016/j.cpc.2019.107129

Wolfram Alpha. (2023). *Integral of* $\sin^{3/2}(x)$ *from 0 to* π. `https://www.wolframalpha.com/input?i=integral+of+sin%5E%283%2F2%29%28x%29+from+0+to+pi`. (Accessed 20th March 2023)